nature plants

Article

https://doi.org/10.1038/s41477-025-01948-4

Satellite-based evidence of recent decline in global forest recovery rate from tree mortality events

Received: 14 June 2024

Accepted: 21 February 2025

Published online: 18 April 2025

Check for updates

Yuchao Yan[1,2,11], Songbai Hong[3,11], Anping Chen[4] ✉, Josep Peñuelas[5,6], Craig D. Allen[7], William M. Hammond[8], Seth M. Munson[9], Ranga B. Myneni[10] & Shilong Piao[1] ✉

Climate-driven forest mortality events have been extensively observed in recent decades, prompting the question of how quickly these affected forests can recover their functionality following such events. Here we assessed forest recovery in vegetation greenness (normalized difference vegetation index) and canopy water content (normalized difference infrared index) for 1,699 well-documented forest mortality events across 1,600 sites worldwide. By analysing 158,427 Landsat surface reflectance images sampled from these sites, we provided a global assessment on the time required for impacted forests to return to their pre-mortality state (recovery time). Our findings reveal a consistent decline in global forest recovery rate over the past decades indicated by both greenness and canopy water content. This decline is particularly noticeable since the 1990s. Further analysis on underlying mechanisms suggests that this reduction in global forest recovery rates is primarily associated with rising temperatures and increased water scarcity, while the escalation in the severity of forest mortality contributes only partially to this reduction. Moreover, our global-scale analysis reveals that the recovery of forest canopy water content lags significantly behind that of vegetation greenness, implying that vegetation indices based solely on greenness can overestimate post-mortality recovery rates globally. Our findings underscore the increasing vulnerability of forest ecosystems to future warming and water insufficiency, accentuating the need to prioritize forest conservation and restoration as an integral component of efforts to mitigate climate change impacts.

Covering around 30% of the land surface, forests provide multiple key ecosystem services, including carbon sequestration, climate change mitigation, hydrological regulation and biodiversity preservation[1,2]. The capacity of forest ecosystems to provide these ecosystem services with socioeconomic benefits to humans, however, could be undermined by severe drought and heatwaves that have induced extensive forest mortality events in recent decades[2–9]. While substantial research has examined triggers and consequences of these widespread tree mortality events[10–13], our understanding of global post-mortality forest recovery, especially the rate and mechanisms of such recovery, remains limited. Improved understanding of such recovery rates and the underlying factors that can revive forest function is pivotal for guiding forest management strategies and projecting climate change impacts[14,15].

Multiple factors, including elevated temperatures, increasing atmospheric CO_2 concentrations, heightened nitrogen deposition, disturbance severity and site edaphic conditions, can considerably

A full list of affiliations appears at the end of the paper. ✉e-mail: Anping.Chen@colostate.edu; slpiao@pku.edu.cn

influence post-mortality forest recovery. These factors may act in divergent directions. For example, CO_2 fertilization and nitrogen deposition could bolster post-mortality vegetation growth, expediting ecosystem recovery, both directly[16,17] and indirectly through enhanced water-use efficiency[18–20]. By contrast, warming-induced water scarcity[21] and heat-induced photosynthetic suppression[3–5] can impede ecosystem recovery[22]. The combined effects of these factors, however, remain inadequately elucidated at a global scale[23]. In particular, little is known about how various global change factors drive recovery patterns across a range of different site conditions.

To bridge this knowledge gap, we examined post-mortality forest recovery across 1,699 well-documented drought- or heat-induced tree mortality events from 1,600 sites globally that have occurred since the 1980s (Fig. 1a). Leveraging 30 m spatial resolution, Landsat-derived normalized difference vegetation index (NDVI) and normalized difference infrared index (NDII) during the growing season, we estimated post-mortality recovery rates for a 3 × 3 pixel window centred on each of the mortality sites. The selection of NDVI and NDII for this study was based on their distinct sensitivities to vegetation characteristics: NDVI is widely used as a measure of vegetation greenness, making it a valuable indicator of photosynthetic activity and vegetation productivity; NDII is known for its sensitivity to canopy water content, providing insight into vegetation water stress[24,25]. A healthy forest, characterized by optimal greenness and sufficient canopy water content, is more likely to show higher carbon sequestration capabilities, thereby substantially contributing to carbon storage. By examining both NDVI and NDII together, we aimed to capture a comprehensive perspective of vegetation dynamics in the context of forest recovery after tree mortality. The spatial scale covered by this specific 3 × 3 pixel window was validated in our previous study to be the most severely affected by mortality relative to other scales[26]. We defined forest recovery time (RT) as the period required for post-mortality NDVI or NDII values to restore from the lowest values to their pre-mortality values (Methods and Supplementary Fig. 1). By definition, the reciprocal of RT equals forest recovery rate. Through comparing RT values indicated by NDVI versus by NDII, we also shed light on recovery trajectories of different ecosystem functions. Furthermore, we calculated and compared RT values across distinct decades (1980s, 1990s and 2000s) to elucidate potential shifts in global forest recovery patterns and harnessed machine learning algorithms to probe the underlying mechanisms driving RT variations globally. Our comprehensive analysis thus lends insights into vegetation recovery and functional restoration after severe mortality events, improving our mechanistic understanding and prediction of forest ecosystem dynamics under future intensified climate change.

Results

Slower recovery of NDII than NDVI

We found an intriguing temporal mismatch between the recovery of vegetation greenness and canopy water content across the global scale. Specifically, the recovery of NDII lagged considerably behind NDVI recovery (Fig. 1b–d). By 2020, NDVI had regained pre-mortality levels for 92% of the examined mortality events, with an RT of 4.7 years (s.d. = 3.8 years; Fig. 1b). More specifically, NDVI fully recovered within 4 years for 55% of the examined events and within 10 years for 84% of the events. By stark contrast, NDII recovered to pre-mortality levels for only 64% of the mortality events by 2020, with an average RT of 6.7 years (s.d. = 4.8 years). About 24% and 52% of the examined events showed full NDII recovery within 4 and 10 years, respectively. This higher percentage of unrecovered NDII than NDVI was also evident for mortality events occurring in all the decades after the 1980s (Fig. 1c inset). In cases where both NDVI and NDII achieved full recovery by 2020, NDII consistently required more or at least equal time to recover than NDVI (Fig. 1c). Over the studied decades, the average RT values for NDII were significantly greater than those for NDVI (Fig. 1d; $P < 0.001$ in two-side paired Student's t-test). It is worth noting that mean RT disparities between NDVI and NDII were 1.8, 3.3, 3.0 and 1.8 years for the 1980s, 1990s, 2000s and 2010s, respectively, and the overall RT disparity for all the decades combined was 2.6 years. Taken together, these results signify a slower recovery in canopy water content than in greenness. This finding aligns with previous studies conducted at local scales[27–29] and provides new insight at a global scale of an important mismatch.

The distinct recovery patterns observed between NDVI and NDII highlight that the resurgence of vegetation greenness does not necessarily equate to the restoration of canopy water content, much less physiological functions (for example, photosynthesis, transpiration and nutrient uptake). The rapid post-mortality recovery of greenness can be attributed to several factors, including the growth recovery of surviving trees, the regeneration of young trees, and the flourishing growth of understory vegetation such as shrubs or herbaceous plants[30]. However, even when similar levels of greenness are restored, these younger saplings and the understory vegetation may not yet achieve the same physiological functions as the pre-mortality vegetation. This was corroborated by research on Siberian Forest post-fire vegetation regeneration using L-band vegetation optical depth derived from passive microwave observations[31], which also indicated that the recovery of greenness does not equate to the recovery of carbon storage. Moreover, while long-term greening trends are often observed at sites where tree mortality events have occurred[26], comprehensive recovery of ecosystem functions may require several decades, as shown by site-specific studies[32], regional assessments[33] and continental-scale investigations[31]. The asynchronous recovery between greenness and canopy water content could be influenced by vegetation structure, such as the leaf area index (LAI) and stand dynamics (Methods). Our analysis delves into the fluctuations of NDVI and NDII concerning LAI (Supplementary Fig. 2a–f), indicating a saturation effect that might contribute to the distinctive recovery patterns observed between NDVI and NDII datasets (Methods). In addition, younger stands, characterized by higher tree density and potentially greater water stress compared to older stands[34], could also result in a scenario where NDVI shows a rapid recovery while NDII exhibits a delayed recovery after mortality (Methods). Therefore, while the restoration of greenness serves as an indicator for the start of physiological function recovery, focusing on greenness alone may lead to an underestimation of the adverse impacts of forest mortality on ecosystem structure and function and overestimation of forest recovery rate.

Declining recovery rates of NDVI and NDII

The nearly 40 year time series data of NDVI and NDII also allow us to assess how post-mortality forest recovery may have changed over the past few decades. In this Article, we compared RT across different mortality decades (1980s, 1990s and 2000s) for both NDVI and NDII. We considered equitable time frames in each decade to assess recovery by selecting specific cut-off years (Methods and Supplementary Table 1). For instance, we computed RT and the unrecovered percentage for mortality events occurring in the 1980s using a 2010 cut-off year, and a 2020 cut-off year for those occurring in the 1990s. We did not observe any statistically significant differences in RT between the 1980s and the 1990s for either NDVI or NDII (Fig. 2a,c). However, a significant prolongation of forest recovery was found from the 1990s to the 2000s (Fig. 2b,d). Specifically, NDVI RT for mortality events in the 2000s was 6.5 years, significantly higher ($P < 0.05$, one-way analysis of variance (ANOVA)) than the RT value of 4.4 years for those in the 1990s (Fig. 2b). Similar results were found for NDII (8.8 years in the 2000s versus 5.9 years in the 1990s, $P < 0.05$; Fig. 2d). In addition, the unrecovered percentage for NDII also increased from 23% in the 1990s to 47% in the 2000s (Fig. 2d, red segment of ring). To further validate these findings, we conducted additional comparisons of RTs by ensuring the number of years included for assessing RT were the same (that is, 20 years) across all three decades. The results reaffirmed

https://doi.org/10.1038/s41477-025-01948-4

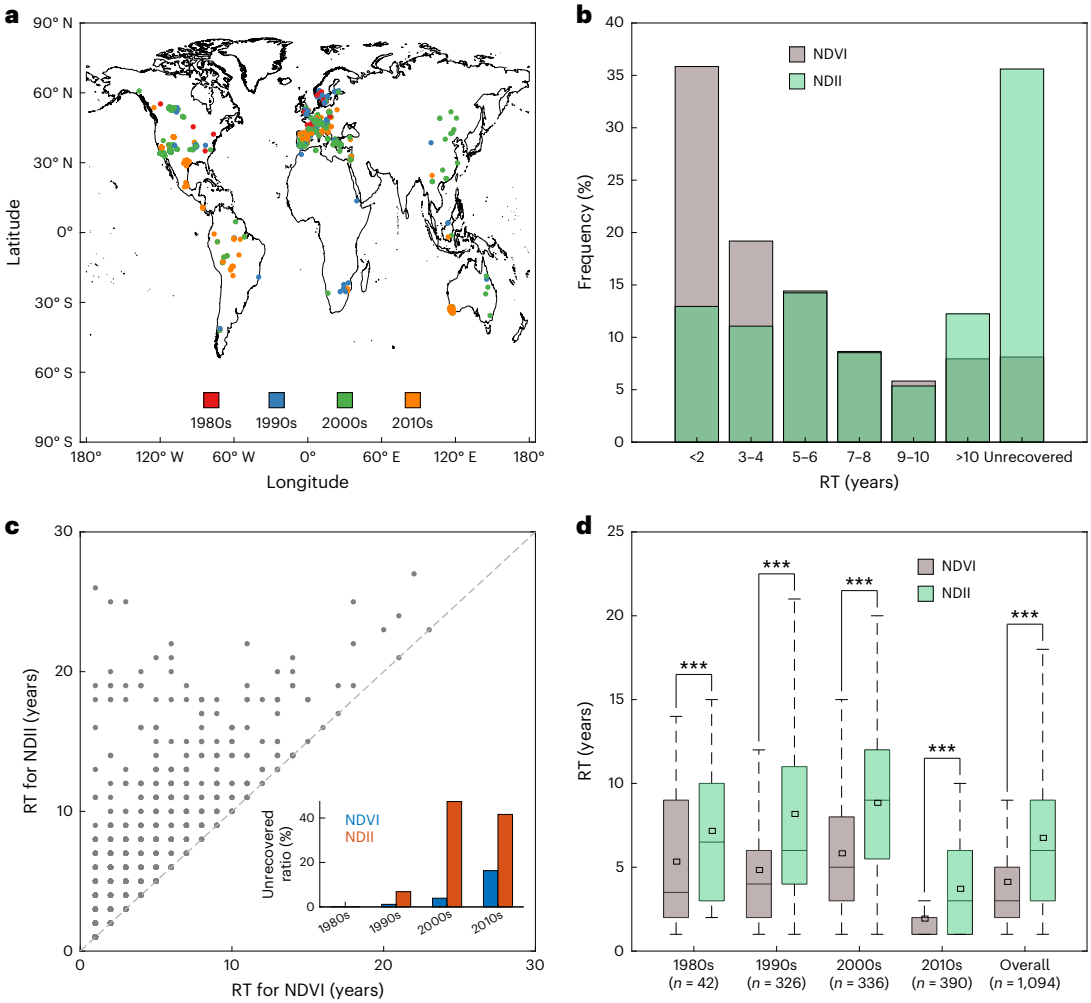

Fig. 1 | Recovery of NDVI and NDII after tree mortality events. a, Spatial distribution of the tree mortality sites included in the study. Different colours indicate the decades when tree mortality occurred. The world continental boundaries were sourced from the Environmental Systems Research Institute World Continents dataset at https://hub.arcgis.com/datasets/esri::world-continents/about. **b**, Frequency distributions of the RT for NDVI and NDII. Dark green colour in the bar chart represents the overlapping portion between NDVI and NDII. **c**, Comparison of RT for NDVI and NDII. The dashed line corresponds to equal (1:1) NDVI and NDII values. There are no points below this dashed line. In the inset, bars indicate the unrecovered ratio of NDVI (blue) and NDII (red) for mortality events that occurred in different decades. **d**, Comparison of RT for NDVI and NDII by decade of the mortality events. ***$P < 0.001$), significant difference in average RT between NDVI and NDII based on a two-sided paired *t*-test, for the following decades: 1980s ($P = 9.85 \times 10^{-6}$), 1990s ($P < 1 \times 10^{-16}$), 2000s ($P < 1 \times 10^{-16}$) and 2010s ($P < 1 \times 10^{-16}$); overall data ($P < 1 \times 10^{-16}$). In the box plot, the top and bottom edges represent the 25th and 75th percentiles of the data, respectively. The whiskers indicate the maximum and minimum values within the non-outliers' range. The horizontal line inside the box indicates the median value. The square inside the box indicates the average value.

the notable prolongation of forest recovery, evident for both NDVI and NDII, from the 1990s to the 2000s (Supplementary Fig. 3).

Next, we investigated whether this delay was independent of local climate conditions by comparing RT values across decades. We found a widespread increase in RT from the 1990s to the 2000s across climate spaces defined by long-term (1980–2020) mean annual temperature (MAT) and mean annual precipitation (MAP) for both NDVI and NDII (Supplementary Fig. 4). We also conducted further analysis on the temporal variation in RT for different research hotspots. In Europe, where the majority of the documented mortality events were concentrated, RT showed a notable increase from the 1980s to the 2000s for both NDVI and NDII (Fig. 2e). The exception was for NDVI derived RT between the 1980s and the 1990s, when the observed increase lacked statistical significance. In North America, a marked increase in RT was evident between the 1990s and the 2000s, whereas we found no statistically significant difference between the 1980s and the 1990s (Supplementary Fig. 5a,c). For tropical forests, where the loss of ecosystem resilience has attracted widespread attention[13,35,36], we were only able to compare RT during the 1990s and 2000s due to the paucity of mortality event reports (Supplementary Fig. 5b,d). The results showed a slight yet statistically nonsignificant increase in RT for both NDVI and NDII. Moreover, we assessed the recovery of NDVI and NDII across different forest biomes, including deciduous broadleaf forest (DBF), evergreen needleleaf forest (ENF), and shrubland (Supplementary Fig. 6). Once again, the outcomes align with our initial findings, indicating a pronounced extension in forest recovery for both NDVI and NDII from the 1990s to the 2000s.

We further tested the robustness of our findings through aggregating data from a 5 × 5 pixel window instead of a 3 × 3 pixel window (Supplementary Fig. 7 and Methods). The results reaffirmed that NDII-based RT values generally exceeded those based on NDVI (Supplementary Fig. 7a), confirming that canopy water content recovery takes longer than greenness recovery. Moreover, we also found an evident prolongation of post-mortality RT, particularly between the 1990s and 2000s (Supplementary Fig. 7b–d). Thus, the two key findings of our research conducted at a global scale, including both the longer time

https://doi.org/10.1038/s41477-025-01948-4

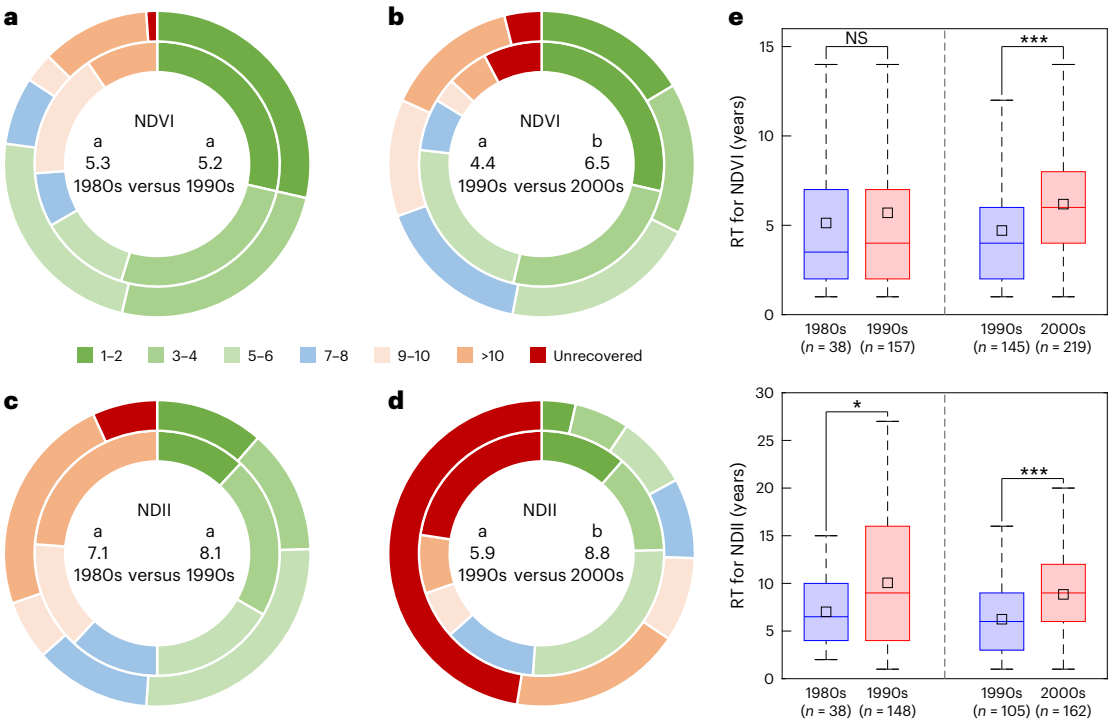

Fig. 2 | Comparison of RT after tree mortality events among different decades. **a**, Comparison of global RT of NDVI between the 1980s and 1990s. The inner ring indicates frequency distribution of RT following tree mortality in the 1980s ($n = 42$), while the outer ring indicates the distribution in the 1990s ($n = 346$). The numbers inside both rings indicate the respective mean RT values, and the same letter 'a' above each number indicates no significant difference between two decades based on a one-way ANOVA. **b**, Comparison of global NDVI RT between the 1990s ($n = 323$) and 2000s ($n = 614$), with the same explanation as in **a** except that different letters 'a' and 'b' indicate significant differences ($P = 3.78 \times 10^{-16}$) in the average NDVI RT. **c**, Comparison of global NDII RT between the 1980s ($n = 42$) and 1990s ($n = 326$), with the same explanation as in **a**. **d**, Comparison of global NDII RT between the 1990s ($n = 271$) and 2000s ($n = 336$), with the same explanation as in **a** except that different letters 'a' and 'b' indicate significant differences ($P = 9.91 \times 10^{-20}$) in the average NDII RT. **e**, Comparison of RT for NDVI and NDII in Europe among different decades. Europe was selected as a typical area due to the large sample size available. ***$P < 0.001$ and *$P < 0.05$, significant differences between two groups based on a one-way ANOVA. This includes significant differences in the average NDVI RT between the 1990s and 2000s ($P = 9.95 \times 10^{-5}$), in the average NDII RT between the 1980s and 1990s ($P = 0.0108$), and in the average NDII RT between the 1990s and 2000s ($P = 8.45 \times 10^{-8}$). NS, not significant. In the box plot, the top and bottom edges represent the 25th and 75th percentiles of the data, respectively. The whiskers indicate the maximum and minimum values within the non-outliers' range. The horizontal line inside the box indicates the median value. The square inside the box indicates the average value.

required for restoring canopy water content and the recent decline in global forest recovery rate, were robust with the choice of different pixel window sizes.

Potential causes of the recent declining recovery

There may be numerous mechanisms underlying the observed delay in forest recovery. We thus used a fusion of extreme gradient boosting (XGBoost) and Shapley additive explanation (SHAP) models[37–39], incorporating 19 factors tied to climate, soil, vegetation, topography and mortality severity, to reveal the major influencing factors governing post-mortality forest recovery (Fig. 3 and Methods). These models showed acceptable efficacy in simulating NDVI- and NDII-based RT values ($R^2 = 0.65$ to 0.89, root mean square error = 0.13 to 0.22; Supplementary Fig. 8). Unsurprisingly, mortality severity played a role in affecting RT for both NDVI (Fig. 3a) and NDII (Fig. 3h), with greater severity linked to extended RT (Fig. 3c,m). Climatic factors, including MAT, MAP of mortality-affected sites, temperature anomaly during RT (*Tem* in RT = mean temperature during RT − MAT) and precipitation anomaly during RT (*Pre* in RT = (mean precipitation during RT − MAP)/MAP × 100%), showed strong influence on post-mortality forest recovery. Specifically, a higher MAT corresponded to reduced RT for both NDVI (Fig. 3b) and NDII (Fig. 3j), indicating faster recovery in warmer regions. However, elevated temperatures during the recovery period impeded forest recuperation, as indicated by the positive correlation between *Tem* in RT and RT, albeit with a nonlinear relationship (Fig. 3d,k). Despite the nonlinear nature of the effect of *Pre* in RT on RT, it was evident that wetter-than-average recovery conditions promoted forest recovery (Fig. 3e,i). NDVI- and NDII-based RT peaked at mid-elevations (Fig. 3f,n) and lower specific leaf area (SLA) (Fig. 3g,l). To assess the impact of spatial-scale discrepancies among independent variables on these findings, we conducted two types of analysis—aggregating both dependent and independent variables from mortality sites into a common grid of coarse pixels (0.5° or approximately 55 km) and randomly selecting one tree mortality site within each coarse pixel—and then re-ran the machine learning model (Methods). We consistently observed similar outcomes (the dominant factors explaining variation in Supplementary Figs. 9 and 10), suggesting that different resolutions of independent variables did not confound our findings.

Given the paramount influence of mortality severity and climate variables on post-mortality forest recovery (Fig. 3a,h), we proposed two hypotheses which are not necessarily mutually exclusive. First (H1), the delay in forest recovery during recent decades was driven by an increase in mortality severity. Second (H2), the prolonged recovery was primarily caused by the changes in climate during the recovery period. To facilitate understanding, we combined the results of Fig. 2 and Supplementary Figs. 5, 11 and 12 into a table (Table 1) for testing these hypotheses. To test hypothesis H1, we contrasted mortality severity across decades (Table 1 and Supplementary Fig. 11). At the global scale, the significant increase in NDII-based mortality severity from the 1980s to 1990s may have played a role in the increase in NDII-based RT, although it is nonsignificant (Table 1, Fig. 2 and Supplementary Fig. 11a). However, the nonsignificant changes in NDVI-based and

https://doi.org/10.1038/s41477-025-01948-4

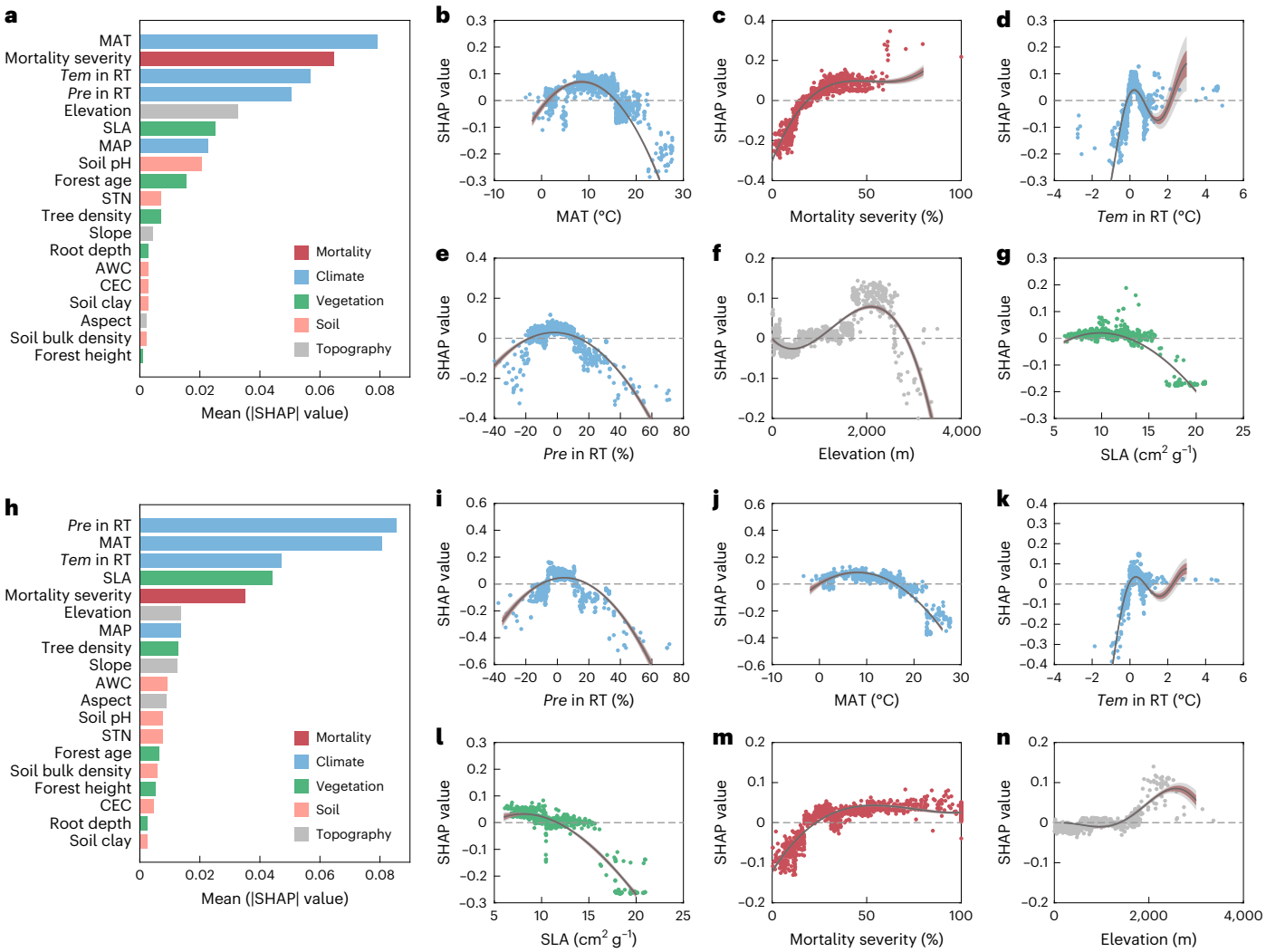

Fig. 3 | Potential drivers affecting RT. a,**h**, The relative importance of mortality, climate, vegetation, soil, and topographic factors for RT of NDVI (**a**) and NDII (**h**). The importance was assessed with the mean |SHAP| value. **b**–**g**,**i**–**n**, Partial dependence plots of the SHAP value against the six most important explanatory variables in **a** (MAT (**b**), mortality severity (**c**), *Tem* in RT (**d**), *Pre* in RT (**e**), elevation (**f**) and SLA (**g**)) and **h** (*Pre* in RT (**i**), MAT (**j**), *Tem* in RT (**k**), SLA (**l**), mortality severity (**m**) and elevation (**n**)). SHAP > 0 means that the corresponding driver positively affected the dependent variable, and SHAP < 0 is a negative effect. The dark grey line represents the fitted line, providing an estimate of the general trend within the dataset. The pink shadings depict the 95% confidence interval of the mean estimate, indicating the range where there is a 95% confidence level that the actual population mean is found. The medium grey shadings show the 95% prediction interval, suggesting that approximately 95% of observations are likely to fall within this specific range. AWC, available water capacity. Mortality severity was defined as the decline magnitude in NDVI and NDII during tree mortality events relative to pre-mortality values.

NDII-based mortality severity from the 1990s to 2000s fails to explain the corresponding significant increase in NDVI-based and NDII-based RT, respectively. Furthermore, in Europe, the region with the most extensive mortality records, the NDVI-based mortality severity contradicted changes in NDVI-based RT between the 1980s and 2000s, and NDII-based mortality severity contradicted changes in NDII-based RT between the 1980s and 1990s (Table 1, Fig. 2 and Supplementary Fig. 11b). Similarly, in North America, changes in both NDVI-based and NDII-based mortality severity contradicted changes in their respective RT between the 1980s and 2000s (Table 1, Supplementary Fig. 5 and Supplementary Fig. 11c). Hence, changes in mortality severity could only partly explain the delay in post-mortality recovery at regional and global scales. Nonetheless, it should be noted that reductions in NDVI and NDII may not fully capture the damage to plant physiology during mortality events, particularly to the root systems.

We found evidence consistently supporting hypothesis H2 from the analysis of climatic conditions during recovery periods (Table 1 and Supplementary Fig. 12). At both global and European scales, changes in *Tem* in RT from the 1980s to the 1990s were trivial and statistically nonsignificant, aligning with the little change in RT; the notable rise in *Tem* in RT was consistent with a significant increase in NDVI-based and NDII-based RT observed from the 1990s to the 2000s (Table 1, Fig. 2, and Supplementary Fig. 12a). A significant decrease in *Pre* in RT between the 1990s and the 2000s was also observed (Table 1 and Supplementary Fig. 12c), indicating that rising temperatures and reduced precipitation during recovery played a crucial role in the recent slow-down in post-mortality recovery rates. In North America, the increase in RT from the 1990s to the 2000s was likely a result of decreased *Pre* in RT (Table 1, Supplementary Fig. 5 and Supplementary Fig. 12d), while the increase in *Tem* in RT lacked statistical significance (Table 1 and Supplementary Fig. 12b).

To test the robustness of our findings as presented in Table 1, we conducted an in-depth analysis using generalized linear mixed models[40] to better elucidate the relationships among mortality severity, temperature, precipitation and RT (Supplementary Tables 2–5). Our analysis revealed that the coefficients of *Pre* in RT and *Tem* in RT

https://doi.org/10.1038/s41477-025-01948-4

Table 1 | Evidence for testing hypotheses H1 and H2

	Global		Europe		North America		Tropic
	1980s vs 1990s	1990s vs 2000s	1980s vs 1990s	1990s vs 2000s	1980s vs 1990s	1990s vs 2000s	1990s vs 2000s
NDVI-based RT	⇩	⬆	⇧	⬆	⇩	⬆	⇧
NDII-based RT	⇧	⬆	⬆	⬆	⇩	⬆	⇧
Tem in RT	⇧	⬆	⇩	⬆	⇧	⇧	⇧
Pre in RT	⇧	⬇	⬆	⬇	⬆	⬇	⇧
NDVI-based mortality severity	⇩	⇩	⬇	⇩	⇧	⇩	⇧
NDII-based mortality severity	⬆	⇩	⇩	⇩	⬆	⬇	⇧

This table summarizes the results of Fig. 2 and Supplementary Figs. 5, 11 and 12. ⬆ represents a significant increase ($P<0.05$, one-way ANOVA), while ⬇ represents a significant decrease ($P<0.05$, one-way ANOVA); ⇧ represents nonsignificant increase, while ⇩ represents nonsignificant decrease. NDVI-based and NDII-based mortality severity are indicated by NDVI and NDII decline magnitudes during mortality events, respectively.

are notably larger than that of mortality severity. This suggests that the decline in global forest recovery rates is predominantly influenced by increasing temperatures and heightened water scarcity. In comparison, the impact of forest mortality severity on this decline appears to be much less. It is also noteworthy that the interaction between *Pre* in RT and *Tem* in RT strongly regulated RT. The results derived from our generalized linear mixed models are consistent with the conclusions drawn from Table 1 and Fig. 3, providing a more robust statistical foundation to support our findings.

Discussion

These findings highlight that the pace of recovery in forest ecosystems following mortality events has been hindered by climate warming and water scarcity. While the direct impact of fertilization of increased CO_2 and nitrogen deposition and its water conservation benefits can boost recovery, this positive effect could have been outweighed by the adverse effects of climate warming and water scarcity[41–44]. Indeed, there is growing evidence that global ecosystems are transitioning from a period dominated by fertilization effects to that dominated by warming effects[23], a shift further supported by our recovery-focused results. Together, these indicate that the net terrestrial ecosystem carbon sink in the past decades due to anthropogenic fertilization of the Earth with increasing concentrations of atmospheric CO_2 and nitrogen inputs is slowing down because of the increasing limitations of water and heat, among other factors[43]. With climate change, the prospects of heightened high-temperature stress and increased water scarcity loom[45], potentially threatening the carbon storage capacity of forest ecosystems. This is particularly concerning due to the heightened risk of forest mortality and a hindered recovery process.

The extension of post-mortality recovery durations in the 2000s compared to earlier decades may also be partially attributed to other factors[23]. Among these factors, diminishing nitrogen availability in terrestrial ecosystems, especially in Europe and North America[46,47], and signs of phosphorus scarcity as a limitation for vegetation growth[48,49] may impede secondary succession and slow down recovery from mortality events[23]. This is despite our models suggesting that soil total nitrogen (STN) and cation exchange capacity (CEC) have weak effects on RT across different regions (Fig. 3a,h).

Moreover, interactions with other climate-related disturbance processes and increased human disturbances in recent decades—including fire, land use change and forest harvesting—could also modify and hinder vegetation recovery after mortality events and thus contribute to the decline in recovery rates[23,50,51]. These alterations may have important impacts on stand dynamics, affecting the recovery of vegetation indices. Such altered or novel disturbance regimes and human disturbance processes can interact with climate warming, water scarcity, and nutrient limitations, adding complexity to the outcomes of forest recovery[52], which merits further investigation.

While numerous studies have been conducted on the rising incidence of forest mortality events[3–7,9,53,54], there is a lack of knowledge regarding the influence of different global change factors on recovery patterns following such events. Our study offers insights into global-scale post-mortality forest recovery trajectories and sheds light on the declining recovery rates in both greenness and canopy water content. These findings highlight a long-term threat posed by heat stress and water scarcity to ecosystem health. Nevertheless, there are still challenges to fully comprehend the intricacies of post-mortality recovery. Field records of mortality events in tropical and boreal forests remain relatively scarce[5], hindering a more complete characterization of post-mortality forest dynamics in these vulnerable regions under climate change[41,55]. Furthermore, it is important to acknowledge the limitations of relying solely on indirect measurements—specifically, remotely sensed indices—for all interpretations. First, the observed decline in post-mortality forest recovery rates, possibly influenced by the inclusion of specific decades (1980s, 1990s and 2000s), may not reflect a long-term trend due to the restricted time frame (no reliable imagery before 1984) of the Landsat dataset to definitively support a consistent decline in global forest recovery rates. Second, although the impact of inconsistencies between different generations of Landsat sensors on ratio-based vegetation indices, as noted by ref. 56, is minimal and has a limited effect on our research results, it is essential to recognize the existence of these discrepancies. Third, satellite-based data do not fully capture changes in vegetation physiological processes. Hence, there is a pressing need for future efforts to establish extensive and long-term field monitoring of post-mortality recovery in both forest structures and functions. Incorporating these detailed observations such as vegetation regrowth rates into process-based models will strengthen our understanding of the multifaceted characteristics of post-mortality forest recovery by various factors. This integration will lead to a more comprehensive mechanistic understanding and enable more accurate projections of forest dynamics in response to changing climate.

We are also aware of potential limitations in our machine learning analyses that stem from differences in spatial resolutions across different data sources. The climate, soil and vegetation attribute data have relatively coarse spatial resolutions at a global scale, posing challenges in aligning them with the finer 30 m resolution Landsat data. While we partially tackled this issue by adopting two analytical methods—aggregating both dependent and independent variables from mortality sites into a common grid of coarse pixels and randomly selecting one tree mortality site within each coarse pixel—there is still room for improvement. Future research should explore integrating higher-resolution data for climate, soil, vegetation attributes and topography, which may offer deeper insights into the mechanisms governing forest recovery dynamics following mortality events.

Conclusions

In summary, our investigation encompassing satellite-derived NDVI and NDII data across 1,600 sites affected by 1,699 mortality events globally has revealed a decline in post-mortality forest recovery rate in recent decades. This decline in forest recovery was primarily influenced by rising temperatures and reduced precipitation during the recovery phase, while changes in mortality severity played a lesser role. Our study also underscores the urgent threat of future climate warming and water scarcity to the maintenance of forest ecosystem functions and the essential services they provide. It thus highlights the critical need to address climate change and implement effective forest management measures to mitigate its negative effects.

Moreover, our global-scale analysis further suggests that the recovery of NDII, an indicator of canopy water content, was more protracted compared to the recovery of NDVI, a metric of vegetation greenness. Thus, the relatively swift restoration of post-mortality vegetation greenness—likely facilitated by the rapid growth of understory vegetation and young trees after the removal of large canopy trees—does not necessarily signify complete recovery of forest ecosystem functions. Consequently, investigations focusing solely on vegetation greenness are likely insufficient for comprehending post-mortality vegetation dynamics. A more holistic understanding of forest ecosystem recovery responses to drought- and heat-induced tree mortality events requires assessments of multiple indices associated with distinct ecosystem functions.

Methods

Dataset of tree mortality events

We evaluated global forest recovery following mortality events induced by combinations of drought and heat in this study. The global dataset of tree mortality sites was initially compiled by ref. 5, encompassing a total of 1,303 sites where tree mortality events related to drought and heat (excluding fire) occurred between 1970 and 2018. These sites were identified based on data collected from 154 peer-reviewed publications, which provided information on the geographical locations and timing of each mortality event. Tree mortality events in the datasets are determined based on the proportion of standing dead trees in relation to total number of trees in a stand, with a threshold of 15% or higher (for mature trees) considered 'higher than expected'[5]. For more detailed information, refer to the publication by ref. 5 and visit the following link: https://www.tree-mortality.net/globaltreemortalitydatabase/.

We also gathered information on tree mortality events from a georeferenced database developed by ref. 57. This database includes 293 tree mortality sites in European forests that were induced by heat and drought stress during the period from 1970 to 2019. This database was compiled from 69 studies. Furthermore, ref. 58 have recently updated this database by including data from 17 additional tree mortality sites, primarily located in the Mediterranean Basin. The authors provided coordinates for these 310 mortality sites and also indicated the starting and ending years of drought or heat and mortality based on their observations.

By combining these two datasets and incorporating an additional 15 mortality sites obtained from peer-reviewed studies[5], we created a comprehensive dataset comprising 1,628 tree mortality sites, each containing one or more recorded mortality events. It is important to note that we excluded 28 tree mortality sites from the 1970s from our analysis due to a lack of remote sensing data. Consequently, our final dataset for analysis consists of 1,600 sites with a total of 1,699 tree mortality events. Out of these, only 99 sites experienced repeated mortality events. To address the impact of repeated mortality events, we ensured that the NDVI and NDII values had fully recovered from the first mortality impact before analysing the effects of subsequent mortality events. This approach was implemented to mitigate the influence of repeated mortality events on the recovery process following the first impact.

Calculation of Landsat-based NDVI and NDII

NDVI is an indicator of vegetation greenness, while NDII is sensitive to the water content within the vegetation canopy. Both metrics have been extensively used to assess the responses of terrestrial vegetation to drought and/or heat stress[25,59,60]. The formulas for NDVI and NDII are as follows:

$$\mathrm{NDVI} = \frac{\rho_{\mathrm{NIR}} - \rho_{\mathrm{Red}}}{\rho_{\mathrm{NIR}} + \rho_{\mathrm{Red}}} \quad (1)$$

$$\mathrm{NDII} = \frac{\rho_{\mathrm{NIR}} - \rho_{\mathrm{SWIR}}}{\rho_{\mathrm{NIR}} + \rho_{\mathrm{SWIR}}} \quad (2)$$

where ρ_{NIR}, ρ_{Red}, and ρ_{SWIR} represent the near-infrared, red and shortwave infrared spectral bands, respectively. To capture the patchy nature of tree mortality events and accurately characterize vegetation recovery patterns, it is essential to use high-resolution satellite data. We calculated NDVI and NDII at a 30 m resolution using Landsat retrievals, which are well suited for regional-to-global-scale time-series analysis and to our objective.

Landsat time series analysis has been used to quantify forest recovery after disturbances and has been validated as a robust method in many previous studies[61–64]. We used high-level surface reflectance products obtained from three different Landsat sensors: Landsat 5 Thematic Mapper (TM), Landsat 7 Enhanced Thematic Mapper Plus (ETM+) and Landsat 8 Operational Land Imager (OLI). The surface reflectance from Landsat 5 and 7 has been atmospherically corrected using the Landsat Ecosystem Disturbance Adaptive Processing System (LEDAPS) developed by refs. 65,66, respectively. For Landsat 8, the surface reflectance has been atmospherically corrected using the Landsat Surface Reflectance Code developed by ref. 67. These correction methods ensure accurate measurements of surface reflectance across different Landsat sensors. Moreover, the Landsat surface reflectance products include pixel-scale data quality flags, which provide information about clear-sky, water, snow, cloud or shadow conditions. These flags are determined using the C Function of Mask algorithm developed by ref. 68. By using the quality flag information, we were able to remove the effects of water, snow, clouds and their shadows in the Landsat imagery, ensuring reliable and cloud-free data for our analysis.

In this study, a total of 158,427 Landsat surface reflectance images were used, covering the growing season for different latitudinal bands: April to October for areas north of 23.5 °N, whole years for areas between 23.5 °N and 23.5 °S, and October to April for areas south of 23.5 °S[69–71]. The time period ranged from 1984 to 2020. Specifically, Landsat 5 images were used for the periods from 1984 to 2011, Landsat 7 images were used for the periods from 1999 to 2002, and Landsat 8 images were used for the periods from 2013 to 2020. It is important to note that Landsat 7 imagery is unavailable after 31 May 2003 due to the failure of the scan line corrector. To address this data gap, we used a focal mean function provided by Google Earth Engine (GEE) to fill in the missing Landsat 7 scan line corrector-off images in 2012, ensuring the completeness and continuity of the dataset.

The near-infrared band (ρ_{NIR}) corresponds to the fourth band of the Landsat TM/ETM+ sensor and the fifth band of the Landsat OLI sensor. The red band (ρ_{Red}) corresponds to the third band of the TM/ETM+ sensor and the fourth band of the OLI sensor. The shortwave infrared band (ρ_{SWIR}) corresponds to the fifth band of the TM/ETM+ sensor and the sixth band of the OLI sensor. To ensure consistency across different Landsat sensors (TM, ETM+ and OLI), linear transformations were applied to adjust the bands accordingly[72]. Landsat-based NDVI and NDII values were estimated during the growing season using the adjusted bands, following equations (1) and (2). Consequently, the NDVI and NDII values used in this study represent the average values during the growing season.

To mitigate potential systematic errors in site geolocation, the NDVI and NDII values derived from Landsat imagery were obtained by averaging values from a 3 × 3 pixel window and a 5 × 5 pixel window, respectively, centred on each tree mortality site.

Given the substantial volume of Landsat images involved, a pre-processing and calculation approach was adopted using the JavaScript application programming interface of the GEE platform. GEE, a cloud computing platform renowned for its ability to analyse remote sensing data at a global scale[73–75], facilitated the efficient processing and analysis of Landsat-based NDVI and NDII values.

Changes in NDVI and NDII affected by LAI and stand dynamics

The relationship between NDII and canopy water content is primarily influenced by vegetation structure, specifically LAI[76]. We examined the

changes in NDVI and NDII in relation to LAI using the PROSAIL model[77,78], a radiative transfer emulator that combines the PROSPECT leaf optical properties model (propriétés optiques spectrales des feuilles) with the SAIL canopy bidirectional reflectance model (Scattering by Arbitrarily Inclined Leaves). The PROSAIL model inherently incorporates parameters for various leaf-angle distributions, including planophile, erectophile, plagiophile, extremophile, spherical and uniform. Based on the PROSAIL model simulations for each different leaf angle type, we found the lowest LAI values where NDVI and NDII reached saturation are 3 $m^2 m^{-2}$ and 4.5 $m^2 m^{-2}$, respectively (Supplementary Fig. 2a–f). In comparison, only 9.15% of the tree mortality sites had average annual LAI values exceeding 3 $m^2 m^{-2}$, and just 1.69% had values above 4.5 $m^2 m^{-2}$ (Supplementary Fig. 2h), suggesting that the impact of saturation on our results is likely negligible. This is further supported by an analysis of the relationship between NDVI, NDII and LAI using Moderate Resolution Imaging Spectroradiometer satellite observation data from global tree mortality sites (Supplementary Fig. 2g). The results indicate that the saturation points for NDVI and NDII occurred at approximately LAI = 3 $m^2 m^{-2}$. To further assess the impact of saturation on the assessment of interannual trends, we compared the RTs of NDVI and NDII with the less saturation-prone enhanced vegetation index (EVI). Our analysis revealed a consistent lag in NDII recovery compared to EVI, while EVI showed a recovery pattern similar to NDVI (Supplementary Fig. 13). This finding also suggests that influence of saturation on interannual trends is limited, thereby reinforcing the reliability of our findings. Nevertheless, we have not overlooked the potential effects of saturation on the interannual variations of NDVI and NDII after tree mortality. It is crucial to recognize that the inherent differences between NDII and NDVI may also contribute to the observed lag in this study.

When considering stand dynamics, younger stands may show higher tree density and encounter more pronounced water stress compared to older stands[34]. The high density of young forests can promote rapid increases in vegetation cover over the land surface, leading to an accelerated recovery of NDVI. This acceleration is often associated with increased chlorophyll content in denser vegetation, thereby enhancing NDVI values[79]. On the contrary, young forests might also face elevated stress levels, resulting in a slower recovery of NDII. Influenced by factors such as water constraints, young forests could be more susceptible[8], potentially causing a delayed recovery of NDII. The intense competition for water within high-density young forests can further impede NDII recovery, as trees in these dense stands compete for limited water resources[80]. Consequently, comprehending stand dynamics emerges as a crucial factor in elucidating the distinct recovery patterns observed between NDVI and NDII datasets.

Climatic datasets

Climatic factors are fundamental determinants of vegetation recovery following drought[81–83]. Gridded data of the Standardized Precipitation–Evapotranspiration Index (SPEI) were obtained from SPEIbase v.2.6 (https://digital.csic.es/handle/10261/202305) with a spatial resolution of 0.5° and a monthly temporal resolution[84]. The SPEI dataset includes values for various timescales ranging from 1 to 48 months. In this study, we focused on the 12 month integrated SPEI data as an indicator of vegetation water stress, as these account for the time lag in the hydraulic failure and dieback of woody trees in response to drought stress[85]. To assess annual drought intensity associated with tree mortality, we calculated the average SPEI during the annual growing season. Monthly temperature and precipitation data were obtained from the Climatic Research Unit Time-Series version 4.06 (ref. 86) with a spatial resolution of 0.5°, which is available at https://data.ceda.ac.uk/badc/cru/data/cru_ts. We computed the annual temperature by averaging the temperature values over a 12 month period and the annual precipitation by summing the precipitation values over 12 months. These calculations were performed for the years 1980 to 2020. In addition, we derived the multi-year average temperature and precipitation patterns covering the period from 1980 to 2020. For each tree mortality event, we determined the average temperature and precipitation during the RT (that is, *Tem* in RT and *Pre* in RT). Finally, we obtained the SPEI, temperature and precipitation data for the specific locations of the tree mortality sites from the aforementioned climate datasets using ArcGIS 10.7.

Soil datasets

Soil properties influence vegetation recovery after drought events via regulating soil water content and nutrient availability[87–89]. Global maps of available water storage capacity, CEC, soil bulk density, soil clay content, soil sand content and soil pH were obtained from the Regridded Harmonized World Soil Database v1.2 (ref. 90) (https://daac.ornl.gov/SOILS/guides/HWSD.html), with a spatial resolution of 0.05°. STN data, with a spatial resolution of 1 km, were downloaded from the International Soil Reference and Information Centre (ISRIC) World Soil Information[91] (https://data.isric.org/). Soil information corresponding to the locations of the tree mortality sites was extracted from the gridded data using ArcGIS 10.7 based on their longitude and latitude.

Datasets of tree attributes

The physiological structure and function of trees, represented by attributes such as forest height, root depth, tree density, forest age and SLA, are crucial in determining their ability to recover from drought events[92–94]. Canopy height data were obtained from the Global Forest Canopy Height dataset by ref. 95 available at https://webmap.ornl.gov/ogc/dataset.jsp?dg_id=10023_1. The global maximum rooting depth was acquired from the Global Earth Observation for Integrated Water Resource Assessment (Earth2Observe) dataset at https://doi.org/10.6084/m9.figshare.12047241.v6. Tree density data were obtained from the global ground-based product by ref. 96 accessible at https://elischolar.library.yale.edu/yale_fes_data/1/. Global forest age data were downloaded from the Data Portal of the Max Planck Institute for Biogeochemistry by ref. 97 available at https://doi.org/10.17871/ForestAgeBGI.2021. Global map of SLA was downloaded from the TRY Plant Trait Database by ref. 98 accessible at https://www.try-db.org/. All these tree attribute datasets had a spatial resolution of 1 km and were extracted based on the locations of the tree mortality sites using ArcGIS 10.7. In addition, the forest biomes were classified as DBF, ENF and shrubland based on the European Space Agency/Climate Change Initiative Land Cover (http://maps.elie.ucl.ac.be/CCI/viewer/). The LAI data used in this study were obtained from the MOD15A2H.061 product (https://lpdaac.usgs.gov/products/mod15a2hv061/), which is one of the most widely recognized global LAI datasets. This product provided the observed LAI values for each tree mortality site. While 30 m resolution Landsat LAI data would have offered finer spatial detail, such a global dataset is currently unavailable. The Moderate Resolution Imaging Spectroradiometer-derived NDVI and NDII data were downloaded from the MOD13A1.061 product (https://lpdaac.usgs.gov/products/mod13a1v061/).

Topographical datasets

Topographic factors, such as slope, aspect and elevation, generate spatial heterogeneity in landscapes, impacting the distribution and availability of water and heat resources. These factors are instrumental in shaping the patterns of post-drought recovery[99–101]. Elevation, slope and aspect data were obtained from the Shuttle Radar Topography Mission 30 m resolution digital elevation model[102]. To capture the local topographic characteristics around each tree mortality site, we calculated the average elevation, slope and aspect values within a 3 × 3 pixel window and a 5 × 5 pixel window centred on each location. The calculations of these topographical factors were performed using the GEE platform, ensuring accurate and efficient processing of the data.

Calculation of RT and mortality severity

In Supplementary Fig. 1, we illustrate the methodology used to analyse RT from tree mortality events. Following ref. 82, for each tree mortality event, we used the mean values of NDVI and NDII in three consecutive non-drought years (SPEI > −1) before the occurrence of tree mortality as base values ($NDVI_{BV}$ and $NDII_{BV}$). The year when NDVI and NDII reached their lowest values ($NDVI_{LV}$ and $NDII_{LV}$) during tree mortality years was identified as the starting point of recovery. RT for NDVI and NDII was defined as the duration (in years) required for them to recover to their base values ($NDVI_{BV}$ and $NDII_{BV}$) from the year corresponding to $NDVI_{LV}$ and $NDII_{LV}$, respectively. The magnitude of decrease in NDVI and NDII ($NDVI_{DM}$ and $NDII_{DM}$) during the tree mortality years, relative to the pre-mortality base values ($NDVI_{BV}$ and $NDII_{BV}$), was calculated as a measure of mortality severity using the following formulas:

$$NDVI_{DM} = \frac{NDVI_{BV} - NDVI_{LV}}{NDVI_{BV}} \times 100\% \quad (3)$$

$$NDII_{DM} = \frac{NDII_{BV} - NDII_{LV}}{NDII_{BV}} \times 100\% \quad (4)$$

Statistical analysis

A paired Student's *t*-test was used to compare RT values between NDVI and NDII. Differences in RT between decades were evaluated using a one-way ANOVA. It is worth noting that suitable cut-off years were selected for different mortality decades to ensure meaningful comparisons (Supplementary Table 1). For instance, RT and unrecovered percentage for mortality events in the 1980s were calculated using a cut-off year of 2010, while the cut-off year of 2020 was used for the 1990s, ensuring both events had the same recovery period. Similarly, when comparing RT values between the 1990s and 2000s, 2010 was chosen as the cut-off year for mortality events in the 1990s, and 2020 for the 2000s.

To explore the mechanisms underlying the observed variation in RT between NDVI and NDII, we used a combination of the XGBoost and SHAP models. XGBoost is a gradient tree boosting algorithm[37], and SHAP is a method to explain machine learning model outputs and visualize relationships between dependent and driving factors[38,39]. Here SHAP was used to elucidate the complex relationships within the XGBoost model and translate them into interpretable rules. The relative importance of each variable was evaluated using the mean |SHAP| value. The analysis considered 19 independent variables (each with a variance inflation factor of <5 (ref. 103), indicating no multicollinearity) (Supplementary Tables 6 and 7), including mortality-severity indicator, four climate factors, five vegetation factors, six soil factors and three topographic factors. *Tem* in RT was calculated as (mean temperature during RT − MAT) and *Pre* in RT as ((mean precipitation during RT − MAP)/MAP × 100%) to exclude collinearity with MAT and MAP, so that they indicated the temporal dynamics of climate specific to each site. The XGBoost and SHAP models showed strong performance (Supplementary Fig. 8) in simulating RT variations for both NDVI and NDII during the procedures of cross validation (70% of samples for training the model while the remaining 30% for test), making them suitable for exploring the major influencing factors of RT. In addition, to enable cross-site comparisons, we used temporally static values of independent variables at each site, including MAT, MAP, soil properties, forest height, root depth, tree density, forest age and SLA. This approach enabled us to examine how the dependent variable varied across gradients, such as climate, soil and vegetation gradients, of different independent variables. Consequently, all independent variables for a given site remained invariant (for example, MAT representing the long-term (1980–2020) average temperature of a site) to ensure the robustness of spatial analyses.

We conducted these analyses using NDVI and NDII values from a 3 × 3 pixel window and repeated them with a 5 × 5 pixel window to test the robustness of the results (Supplementary Fig. 7). To address spatial-scale mismatch and ensure reliability across resolutions, we performed two additional analyses: (1) data aggregation: When multiple mortality sites fell within the same 0.5° grid, we averaged their values and used the aggregated data in the machine learning model; (2) random sampling: If a 0.5° grid contained multiple sites, we randomly selected one site and used it in the model. We then re-ran the machine learning model for both approaches.

Reporting summary

Further information on research design is available in the Nature Portfolio Reporting Summary linked to this article.

Data availability

The tree mortality sites are available at https://www.tree-mortality.net/globaltreemortalitydatabase/ (ref. 5), https://doi.org/10.3897/oneeco.4.e37753 (ref. 57) and https://doi.org/10.1016/j.scitotenv.2021.151604 (ref. 58). These are summarized and available via figshare at https://doi.org/10.6084/m9.figshare.28375442 (ref. 104). The original NDVI and NDII data are available via figshare at https://doi.org/10.6084/m9.figshare.28375529 (ref. 105). The climate, vegetation and soil data are available via figshare at https://doi.org/10.6084/m9.figshare.28375550 (ref. 106). The world continental boundaries were sourced from the Environmental Systems Research Institute World Continents dataset at https://hub.arcgis.com/datasets/esri::world-continents/about. The temperature and precipitation data can be retrieved from https://data.ceda.ac.uk/badc/cru/data/cru_ts. The SPEI data are available at https://digital.csic.es/handle/10261/202305. The available water storage capacity, CEC, soil bulk density, soil clay and soil pH data were downloaded from https://daac.ornl.gov/SOILS/guides/HWSD.html. The STN can be obtained from https://data.isric.org/. The canopy height can be retrieved from https://webmap.ornl.gov/ogc/dataset.jsp?dg_id=10023_1. The global maximum rooting depth was derived from the Global Earth Observation for Integrated Water Resource Assessment (Earth2Observe) dataset available via figshare at https://doi.org/10.6084/m9.figshare.12047241.v6 (ref. 107). The tree density was derived from https://elischolar.library.yale.edu/yale_fes_data/1/. The forest age data were downloaded from https://doi.org/10.17871/ForestAgeBGI.2021. The SLA data were downloaded from https://www.try-db.org/. The forest biomes were classified as DBF, ENF and shrubland based on the European Space Agency/Climate Change Initiative Land Cover (http://maps.elie.ucl.ac.be/CCI/viewer/). The LAI was obtained from MOD15A2H.061 (https://lpdaac.usgs.gov/products/mod15a2hv061/).

Code availability

Java, MATLAB and Python Codes for the analysis of these data are available via GitHub at https://github.com/YCY-github-YCY/Forest (ref. 108). The Landsat-based NDVI and NDII, and digital elevation model (including elevation, slope and aspect) are calculated on GEE, which is available at https://code.earthengine.google.com/.

References

1. Friedlingstein, P. et al. Global carbon budget 2023. *Earth Syst. Sci. Data* **15**, 5301–5369 (2023).
2. Reid, W. V. et al. *Ecosystems and Human Well-being: Synthesis: A Report of the Millennium Ecosystem Assessment* (Island, 2005).
3. Allen, C. D. et al. A global overview of drought and heat-induced tree mortality reveals emerging climate change risks for forests. *For. Ecol. Manage.* **259**, 660–684 (2010).
4. Allen, C. D., Breshears, D. D. & McDowell, N. G. On underestimation of global vulnerability to tree mortality and forest die-off from hotter drought in the Anthropocene. *Ecosphere* https://doi.org/10.1890/ES15-00203.1 (2015).

5. Hammond, W. M. et al. Global field observations of tree die-off reveal hotter-drought fingerprint for Earth's forests. *Nat. Commun.* **13**, 1761 (2022).
6. Hartmann, H. et al. Research frontiers for improving our understanding of drought-induced tree and forest mortality. *New Phytol.* **218**, 15–28 (2018).
7. Liu, Q. et al. Drought-induced increase in tree mortality and corresponding decrease in the carbon sink capacity of Canada's boreal forests from 1970 to 2020. *Glob. Change Biol.* **29**, 2274–2285 (2023).
8. McDowell, N. G. et al. Pervasive shifts in forest dynamics in a changing world. *Science* **368**, eaaz9463 (2020).
9. Park Williams, A. et al. Temperature as a potent driver of regional forest drought stress and tree mortality. *Nat. Clim. Chang.* **3**, 292–297 (2013).
10. Ratajczak, Z. et al. Abrupt change in ecological systems: inference and diagnosis. *Trends Ecol. Evol.* **33**, 513–526 (2018).
11. Reyer, C. P. et al. Forest resilience and tipping points at different spatio-temporal scales: approaches and challenges. *J. Ecol.* **103**, 5–15 (2015).
12. Smith, T., Traxl, D. & Boers, N. Empirical evidence for recent global shifts in vegetation resilience. *Nat. Clim. Chang.* **12**, 477–484 (2022).
13. Wu, D. et al. Reduced ecosystem resilience quantifies fine-scale heterogeneity in tropical forest mortality responses to drought. *Glob. Change Biol.* **28**, 2081–2094 (2022).
14. Portmann, R. et al. Global forestation and deforestation affect remote climate via adjusted atmosphere and ocean circulation. *Nat. Commun.* **13**, 5569 (2022).
15. Unger, N. Human land-use-driven reduction of forest volatiles cools global climate. *Nat. Clim. Chang.* **4**, 907–910 (2014).
16. Quinn Thomas, R., Canham, C. D., Weathers, K. C. & Goodale, C. L. Increased tree carbon storage in response to nitrogen deposition in the US. *Nat. Geosci.* **3**, 13–17 (2010).
17. Zhu, Z. et al. Greening of the Earth and its drivers. *Nat. Clim. Chang.* **6**, 791–795 (2016).
18. Adams, M. A., Buckley, T. N., Binkley, D., Neumann, M. & Turnbull, T. L. CO_2, nitrogen deposition and a discontinuous climate response drive water use efficiency in global forests. *Nat. Commun.* **12**, 5194 (2021).
19. Huxman, T. E. et al. Convergence across biomes to a common rain-use efficiency. *Nature* **429**, 651–654 (2004).
20. Zhang, Y. et al. Increasing sensitivity of dryland vegetation greenness to precipitation due to rising atmospheric CO_2. *Nat. Commun.* **13**, 4875 (2022).
21. Zhang, Y., Parazoo, N. C., Williams, A. P., Zhou, S. & Gentine, P. Large and projected strengthening moisture limitation on end-of-season photosynthesis. *Proc. Natl Acad. Sci. USA* **117**, 9216–9222 (2020).
22. Tepley, A. J., Thompson, J. R., Epstein, H. E. & Anderson Teixeira, K. J. Vulnerability to forest loss through altered postfire recovery dynamics in a warming climate in the Klamath Mountains. *Glob. Change Biol.* **23**, 4117–4132 (2017).
23. Peñuelas, J. et al. Shifting from a fertilization-dominated to a warming-dominated period. *Nat. Ecol. Evol.* **1**, 1438–1445 (2017).
24. Joiner, J. et al. Global relationships among traditional reflectance vegetation indices (NDVI and NDII), evapotranspiration (ET), and soil moisture variability on weekly timescales. *Remote Sens. Environ.* **219**, 339–352 (2018).
25. Liu, F. et al. Old-growth forests show low canopy resilience to droughts at the southern edge of the taiga. *Glob. Change Biol.* **27**, 2392–2402 (2021).
26. Yan, Y. et al. Climate-induced tree-mortality pulses are obscured by broad-scale and long-term greening. *Nat. Ecol. Evol.* **8**, 912–923 (2024).
27. Chen, X. et al. Detecting post-fire burn severity and vegetation recovery using multitemporal remote sensing spectral indices and field-collected composite burn index data in a ponderosa pine forest. *Int. J. Remote Sens.* **32**, 7905–7927 (2011).
28. Hislop, S. et al. Using Landsat spectral indices in time-series to assess wildfire disturbance and recovery. *Remote Sens.* **10**, 460 (2018).
29. Pickell, P. D., Hermosilla, T., Frazier, R. J., Coops, N. C. & Wulder, M. A. Forest recovery trends derived from Landsat time series for North American boreal forests. *Int. J. Remote Sens.* **37**, 138–149 (2016).
30. Khoury, S. & Coomes, D. A. Resilience of Spanish forests to recent droughts and climate change. *Glob. Change Biol.* **26**, 7079–7098 (2020).
31. Fan, L. et al. Siberian carbon sink reduced by forest disturbances. *Nat. Geosci.* **16**, 56–62 (2023).
32. Larjavaara, M., Berninger, F., Palviainen, M., Prokushkin, A. & Wallenius, T. Post-fire carbon and nitrogen accumulation and succession in Central Siberia. *Sci. Rep.* **7**, 12776 (2017).
33. Berner, L. T. et al. Cajander larch (*Larix cajanderi*) biomass distribution, fire regime and post-fire recovery in northeastern Siberia. *Biogeosciences* **9**, 3943–3959 (2012).
34. Zhang, X., Yu, P., Wang, D. & Xu, Z. Density-and age-dependent influences of droughts and intrinsic water use efficiency on growth in temperate plantations. *Agric. For. Meteorol.* **325**, 109134 (2022).
35. Boulton, C. A., Lenton, T. M. & Boers, N. Pronounced loss of Amazon rainforest resilience since the early 2000s. *Nat. Clim. Chang.* **12**, 271–278 (2022).
36. Verbesselt, J. et al. Remotely sensed resilience of tropical forests. *Nat. Clim. Chang.* **6**, 1028–1031 (2016).
37. Chen, T. & Guestrin, C. XGBoost: A scalable tree boosting system. In *Proc. 22nd ACM SIGKDD International Conference on Knowledge Discovery and Data Mining* 785–794 (Association for Computing Machinery, 2016).
38. Lundberg, S. & Lee, S. A unified approach to interpreting model predictions. In *Proc. 31st International Conference on Neural Information Processing Systems (NIPS'17)* (eds von Luxburg, U. et al.) 4768–4777 (Curran Associates, 2017).
39. Lundberg, S. M. et al. From local explanations to global understanding with explainable AI for trees. *Nat. Mach. Intell.* **2**, 56–67 (2020).
40. Bolker, B. M. et al. Generalized linear mixed models: a practical guide for ecology and evolution. *Trends Ecol. Evol.* **24**, 127–135 (2009).
41. Corlett, R. T. The impacts of droughts in tropical forests. *Trends Plant Sci.* **21**, 584–593 (2016).
42. Nabuurs, G. et al. First signs of carbon sink saturation in European forest biomass. *Nat. Clim. Chang.* **3**, 792–796 (2013).
43. Penuelas, J. Decreasing efficiency and slowdown of the increase in terrestrial carbon-sink activity. *One Earth* **6**, 591–594 (2023).
44. Raupach, M. R. et al. The declining uptake rate of atmospheric CO_2 by land and ocean sinks. *Biogeosciences* **11**, 3453–3475 (2014).
45. Denissen, J. M. et al. Widespread shift from ecosystem energy to water limitation with climate change. *Nat. Clim. Chang.* **12**, 677–684 (2022).
46. Mason, R. E. et al. Evidence, causes, and consequences of declining nitrogen availability in terrestrial ecosystems. *Science* **376**, eabh3767 (2022).
47. Penuelas, J. et al. Increasing atmospheric CO_2 concentrations correlate with declining nutritional status of European forests. *Commun. Biol.* **3**, 125 (2020).
48. Peñuelas, J. et al. Human-induced nitrogen–phosphorus imbalances alter natural and managed ecosystems across the globe. *Nat. Commun.* **4**, 2934 (2013).

49. Wieder, W. R., Cleveland, C. C., Smith, W. K. & Todd-Brown, K. Future productivity and carbon storage limited by terrestrial nutrient availability. *Nat. Geosci.* **8**, 441–444 (2015).
50. Turner, M. G. & Seidl, R. Novel disturbance regimes and ecological responses. *Annu. Rev. Ecol. Evol. Syst* **54**, 63–83 (2023).
51. Zhang, F. et al. Attributing carbon changes in conterminous US forests to disturbance and non-disturbance factors from 1901 to 2010. *J. Geophys. Res. Biogeo.* **117**, G02021 (2012).
52. Seidl, R. & Turner, M. G. Post-disturbance reorganization of forest ecosystems in a changing world. *Proc. Natl Acad. Sci. USA* **119**, e2092777177 (2022).
53. Forzieri, G., Dakos, V., McDowell, N. G., Ramdane, A. & Cescatti, A. Emerging signals of declining forest resilience under climate change. *Nature* **608**, 534–539 (2022).
54. Liu, Y., Kumar, M., Katul, G. G. & Porporato, A. Reduced resilience as an early warning signal of forest mortality. *Nat. Clim. Chang.* **9**, 880–885 (2019).
55. Schuur, E. A. et al. The effect of permafrost thaw on old carbon release and net carbon exchange from tundra. *Nature* **459**, 556–559 (2009).
56. Vogelmann, J. E., Gallant, A. L., Shi, H. & Zhu, Z. Perspectives on monitoring gradual change across the continuity of Landsat sensors using time-series data. *Remote Sens. Environ.* **185**, 258–270 (2016).
57. Caudullo, G. & Barredo, J. I. A georeferenced dataset of drought and heat-induced tree mortality in Europe. *One Ecosyst.* **4**, e37753 (2019).
58. Gazol, A. & Camarero, J. J. Compound climate events increase tree drought mortality across European forests. *Sci. Total Environ.* **816**, 151604 (2022).
59. Klemas, V. & Smart, R. The influence of soil salinity, growth form, and leaf moisture on the spectral radiance of *Spartina alterniflora* canopies. *Photogramm. Eng. Remote Sens.* **49**, 77–83 (1983).
60. Liu, F. et al. Remotely sensed birch forest resilience against climate change in the northern China forest-steppe ecotone. *Ecol. Indic.* **125**, 107526 (2021).
61. Barta, K. A., Hais, M. & Heurich, M. Characterizing forest disturbance and recovery with thermal trajectories derived from Landsat time series data. *Remote Sens. Environ.* **282**, 113274 (2022).
62. Viana-Soto, A. et al. Quantifying post-fire shifts in woody-vegetation cover composition in Mediterranean pine forests using Landsat time series and regression-based unmixing. *Remote Sens. Environ.* **281**, 113239 (2022).
63. White, J. C., Hermosilla, T., Wulder, M. A. & Coops, N. C. Mapping, validating, and interpreting spatio-temporal trends in post-disturbance forest recovery. *Remote Sens. Environ.* **271**, 112904 (2022).
64. White, J. C., Wulder, M. A., Hermosilla, T., Coops, N. C. & Hobart, G. W. A nationwide annual characterization of 25 years of forest disturbance and recovery for Canada using Landsat time series. *Remote Sens. Environ.* **194**, 303–321 (2017).
65. Masek, J. G. et al. A Landsat surface reflectance dataset for North America, 1990–2000. *IEEE Geosci. Remote Sens. Lett.* **3**, 68–72 (2006).
66. Vermote, E. & Saleous, N. *LEDAPS Surface Reflectance Product Description* (University of Maryland, 2007).
67. Vermote, E., Justice, C., Claverie, M. & Franch, B. Preliminary analysis of the performance of the Landsat 8/OLI land surface reflectance product. *Remote Sens. Environ.* **185**, 46–56 (2016).
68. Foga, S. et al. Cloud detection algorithm comparison and validation for operational Landsat data products. *Remote Sens. Environ.* **194**, 379–390 (2017).
69. Peng, X. et al. Northern Hemisphere greening in association with warming permafrost. *J. Geophys. Res. Biogeo.* **125**, e2019JG005086 (2020).
70. Piao, S. et al. Evidence for a weakening relationship between interannual temperature variability and northern vegetation activity. *Nat. Commun.* **5**, 5018 (2014).
71. Wu, X. et al. Higher temperature variability reduces temperature sensitivity of vegetation growth in Northern Hemisphere. *Geophys. Res. Lett.* **44**, 6173–6181 (2017).
72. Roy, D. P. et al. Characterization of Landsat-7 to Landsat-8 reflective wavelength and normalized difference vegetation index continuity. *Remote Sens. Environ.* **185**, 57–70 (2016).
73. Amani, M. et al. Google Earth Engine cloud computing platform for remote sensing big data applications: a comprehensive review. *IEEE J. Sel. Top. Appl. Earth Obs. Remote Sens.* **13**, 5326–5350 (2020).
74. Gorelick, N. et al. Google Earth Engine: planetary-scale geospatial analysis for everyone. *Remote Sens. Environ.* **202**, 18–27 (2017).
75. Tamiminia, H. et al. Google Earth Engine for geo-big data applications: a meta-analysis and systematic review. *ISPRS J. Photogramm. Remote Sens.* **164**, 152–170 (2020).
76. Yilmaz, M. T., Hunt, E. R. Jr & Jackson, T. J. Remote sensing of vegetation water content from equivalent water thickness using satellite imagery. *Remote Sens. Environ.* **112**, 2514–2522 (2008).
77. Baret, F., Jacquemoud, S., Guyot, G. & Leprieur, C. Modeled analysis of the biophysical nature of spectral shifts and comparison with information content of broad bands. *Remote Sens. Environ.* **41**, 133–142 (1992).
78. Jacquemoud, S. et al. PROSPECT+ SAIL models: a review of use for vegetation characterization. *Remote Sens. Environ.* **113**, S56–S66 (2009).
79. Zeng, Y. et al. Optical vegetation indices for monitoring terrestrial ecosystems globally. *Nat. Rev. Earth Environ.* **3**, 477–493 (2022).
80. Brodribb, T. J., Powers, J., Cochard, H. & Choat, B. Hanging by a thread? Forests and drought. *Science* **368**, 261–266 (2020).
81. Li, Y. et al. Widespread spring phenology effects on drought recovery of Northern Hemisphere ecosystems. *Nat. Clim. Chang.* **13**, 182–188 (2023).
82. Schwalm, C. R. et al. Global patterns of drought recovery. *Nature* **548**, 202–205 (2017).
83. Wang, L. Spring phenology alters vegetation drought recovery. *Nat. Clim. Chang.* **13**, 123–124 (2023).
84. Vicente-Serrano, S. M., Beguería, S., López-Moreno, J. I., Angulo, M. & El Kenawy, A. A global 0.5 gridded dataset (1901–2006) of a multiscalar drought index considering the joint effects of precipitation and temperature. *J. Hydrometeorol.* **11**, 1033–1043 (2010).
85. Tong, X. et al. Increased vegetation growth and carbon stock in China karst via ecological engineering. *Nat. Sustain.* **1**, 44–50 (2018).
86. Harris, I., Jones, P., Osborn, T. & Lister, D. Updated high-resolution grids of monthly climatic observations—the CRU TS3. 10 Dataset. *Int. J. Climatol.* **34**, 623–642 (2014).
87. Gessler, A., Schaub, M. & McDowell, N. G. The role of nutrients in drought-induced tree mortality and recovery. *New Phytol.* **214**, 513–520 (2017).
88. Xu, T. et al. Soil property plays a vital role in vegetation drought recovery in karst region of Southwest China. *J. Geophys. Res. Biogeo.* **126**, e2021JG006544 (2021).
89. Yao, Y., Liu, Y., Zhou, S., Song, J. & Fu, B. Soil moisture determines the recovery time of ecosystems from drought. *Glob. Change Biol.* **29**, 3562–3574 (2023).
90. Wieder, W. R., Boehnert, J., Bonan, G. B. & Langseth, M. *Regridded Harmonized World Soil Database v1.2.* (ORNL DAAC, 2014).
91. Batjes, N. H. Harmonized soil property values for broad-scale modelling (WISE30sec) with estimates of global soil carbon stocks. *Geoderma* **269**, 61–68 (2016).

92. Choat, B. et al. Triggers of tree mortality under drought. *Nature* **558**, 531–539 (2018).
93. Fang, O. & Zhang, Q. B. Tree resilience to drought increases in the Tibetan Plateau. *Glob. Change Biol.* **25**, 245–253 (2019).
94. Li, X. et al. Temporal trade-off between gymnosperm resistance and resilience increases forest sensitivity to extreme drought. *Nat. Ecol. Evol.* **4**, 1075–1083 (2020).
95. Simard, M., Pinto, N., Fisher, J. B. & Baccini, A. Mapping forest canopy height globally with spaceborne lidar. *J. Geophys. Res. Biogeo.* **116**, G04021 (2011).
96. Crowther, T. W. et al. Mapping tree density at a global scale. *Nature* **525**, 201–205 (2015).
97. Besnard, S. et al. Mapping global forest age from forest inventories, biomass and climate data. *Earth Syst. Sci. Data.* **2021**, 4881–4896 (2021).
98. Moreno-Martínez, Á. et al. A methodology to derive global maps of leaf traits using remote sensing and climate data. *Remote Sens. Environ.* **218**, 69–88 (2018).
99. Gazol, A., Camarero, J. J., Anderegg, W. & Vicente Serrano, S. M. Impacts of droughts on the growth resilience of Northern Hemisphere forests. *Glob. Ecol. Biogeogr.* **26**, 166–176 (2017).
100. Schwartz, N. B., Budsock, A. M. & Uriarte, M. Fragmentation, forest structure, and topography modulate impacts of drought in a tropical forest landscape. *Ecology* **100**, e02677 (2019).
101. Sturm, J., Santos, M. J., Schmid, B. & Damm, A. Satellite data reveal differential responses of Swiss forests to unprecedented 2018 drought. *Glob. Change Biol.* **28**, 2956–2978 (2022).
102. Farr, T. G. et al. The shuttle radar topography mission. *Rev. Geophys.* **45**, RG2004 (2007).
103. Gareth, J., Daniela, W., Trevor, H. & Robert, T. *An Introduction to Statistical Learning: With Applications in R* (Spinger, 2013).
104. Yan, Y. et al. Tree mortality sites. *figshare* https://doi.org/10.6084/m9.figshare.28375442 (2025).
105. Yan, Y. et al. Recovery of NDVI and NDII. *figshare* https://doi.org/10.6084/m9.figshare.28375529 (2025).
106. Yan, Y. et al. Influencing factors. *figshare* https://doi.org/10.6084/m9.figshare.28375550 (2025).
107. Li, X. et al. Temporal trade-off between gymnosperm resistance and resilience increases forest sensitivity to extreme drought. *figshare* https://doi.org/10.6084/m9.figshare.12047241.v6 (2020).
108. Yan, Y. et al. YCY-github-YCY/Forest. *GitHub* https://github.com/YCY-github-YCY/Forest (2025).

Acknowledgements

This study was supported by the Second Tibetan Plateau Scientific Expedition and Research programme (2024QZKK0301) and the National Natural Science Foundation of China (41988101). A.C. acknowledges support from the US Geological Survey (G22AC00431) and the US Department of Agriculture National Institute of Food and Agriculture (2024-67019-42396). We thank J. Sun, Z. Zeng, Y. Guo and H. Zhuang for their technical assistance in performing PROSAIL model simulations. Any use of trade, firm, or product names is for descriptive purposes only and does not imply endorsement by the US Government.

Author contributions

S.P. and A.C. designed the research. Y.Y. conducted all data processing, calculated RT and ran the model. S.H. and Y.Y. performed statistical analysis and drafted the figures. S.H. and Y.Y. wrote the first draft of the manuscript. W.M.H. collected the tree-mortality sites. Y.Y., S.H., A.C., J.P., S.M.M., C.D.A., W.M.H. and R.B.M. revised the manuscript. All authors discussed the design, methods and results and contributed to the text.

Competing interests

The authors declare no competing interests.

Additional information

Supplementary information The online version contains supplementary material available at https://doi.org/10.1038/s41477-025-01948-4.

Correspondence and requests for materials should be addressed to Anping Chen or Shilong Piao.

Reviewer recognition *Nature Plants* thanks Daniel Kneeshaw and the other, anonymous, reviewer(s) for their contribution to the peer review of this work.

Reprints and permissions information is available at www.nature.com/reprints.

Publisher's note Springer Nature remains neutral with regard to jurisdictional claims in published maps and institutional affiliations.

[1]Institute of Carbon Neutrality, Sino-French Institute for Earth System Science, College of Urban and Environmental Sciences, Peking University, Beijing, China. [2]Guangdong Key Laboratory for Urbanization and Geo-Simulation, School of Geography and Planning, Sun Yat-sen University, Guangzhou, China. [3]School of Urban Planning and Design, Shenzhen Graduate School, Peking University, Shenzhen, China. [4]Department of Biology and Graduate Degree Program in Ecology, Colorado State University, Fort Collins, CO, USA. [5]CREAF, Cerdanyola del Vallès, Spain. [6]CSIC, Global Ecology Unit CREAF-CSIC-UAB, Bellaterra, Spain. [7]Department of Geography and Environmental Studies, University of New Mexico, Albuquerque, NM, USA. [8]Institute of Food and Agricultural Sciences, Agronomy Department, University of Florida, Gainesville, FL, USA. [9]US Geological Survey, Southwest Biological Science Center, Flagstaff, AZ, USA. [10]Department of Earth and Environment, Boston University, Boston, MA, USA. [11]These authors contributed equally: Yuchao Yan, Songbai Hong. ✉e-mail: Anping.Chen@colostate.edu; slpiao@pku.edu.cn

nature portfolio

Corresponding author(s): Anping Chen and Shilong Piao

Last updated by author(s): Feb 13, 2025

Reporting Summary

Nature Portfolio wishes to improve the reproducibility of the work that we publish. This form provides structure for consistency and transparency in reporting. For further information on Nature Portfolio policies, see our Editorial Policies and the Editorial Policy Checklist.

Statistics

For all statistical analyses, confirm that the following items are present in the figure legend, table legend, main text, or Methods section.

n/a	Confirmed	
☐	☒	The exact sample size (*n*) for each experimental group/condition, given as a discrete number and unit of measurement
☒	☐	A statement on whether measurements were taken from distinct samples or whether the same sample was measured repeatedly
☐	☒	The statistical test(s) used AND whether they are one- or two-sided *Only common tests should be described solely by name; describe more complex techniques in the Methods section.*
☒	☐	A description of all covariates tested
☐	☒	A description of any assumptions or corrections, such as tests of normality and adjustment for multiple comparisons
☐	☒	A full description of the statistical parameters including central tendency (e.g. means) or other basic estimates (e.g. regression coefficient) AND variation (e.g. standard deviation) or associated estimates of uncertainty (e.g. confidence intervals)
☐	☒	For null hypothesis testing, the test statistic (e.g. *F*, *t*, *r*) with confidence intervals, effect sizes, degrees of freedom and *P* value noted *Give P values as exact values whenever suitable.*
☒	☐	For Bayesian analysis, information on the choice of priors and Markov chain Monte Carlo settings
☒	☐	For hierarchical and complex designs, identification of the appropriate level for tests and full reporting of outcomes
☒	☐	Estimates of effect sizes (e.g. Cohen's *d*, Pearson's *r*), indicating how they were calculated

Our web collection on statistics for biologists contains articles on many of the points above.

Software and code

Policy information about availability of computer code

Data collection	No software was used to collect data.
Data analysis	The analyses and mapping were both performed using Google earth engine (JavaScript), ArcGIS 10.7, MATLAB (R2020b), and Pycharm 2017.2.7. Codes for processing and analyzing these data can be found in Github (https://github.com/YCY-github-YCY/Forest). C Function of Mask (CFMASK, Version: 3.3) algorithm is a clouds, snow, water, and shadows masking algorithm available in Google Earth Engine. XGBoost is a gradient tree boosting algorithm (Version: 1.4.2), and SHAP is a method to explain machine learning model outputs and visualize relationships between dependent and driving factors (Version: 0.39.0).

For manuscripts utilizing custom algorithms or software that are central to the research but not yet described in published literature, software must be made available to editors and reviewers. We strongly encourage code deposition in a community repository (e.g. GitHub). See the Nature Portfolio guidelines for submitting code & software for further information.

Data

Policy information about availability of data

All manuscripts must include a data availability statement. This statement should provide the following information, where applicable:

- Accession codes, unique identifiers, or web links for publicly available datasets
- A description of any restrictions on data availability
- For clinical datasets or third party data, please ensure that the statement adheres to our policy

The tree mortality sites can be found in Hammond et al. (2022) (https://www.iufro.org/science/task-forces/tree-mortality-patterns), Caudullo and Barredo (2019) (https://doi.org/10.3897/oneeco.4.e37753), and Gazol and Camarero (2022) (https://doi.org/10.1016/j.scitotenv.2021.151604). These are summarized at https://doi.org/10.6084/m9.figshare.28375442. The original NDVI and NDII data can be found at https://doi.org/10.6084/m9.figshare.28375529. The climate, vegetation and soil data can be found at https://doi.org/10.6084/m9.figshare.28375550. The world continental boundaries were sourced from the ESRI World Continents dataset: https://hub.arcgis.com/datasets/esri::world-continents/about. The Landsat-based NDVI and NDII, and DEM (including elevation, slope, and aspect) are calculated on Google Earth Engine, which is available at https://code.earthengine.google.com/. The temperature and precipitation data can be retrieved from https://data.ceda.ac.uk/badc/cru/data/cru_ts. The SPEI data are available from https://digital.csic.es/handle/10261/202305. The available water storage capacity, cation exchange capacity, soil bulk density, soil clay, and soil pH are downloaded from https://daac.ornl.gov/SOILS/guides/HWSD.html. The soil total nitrogen can be obtained from https://data.isric.org/. The canopy height can be retrieved from https://webmap.ornl.gov/ogc/dataset.jsp?dg_id=10023_1. The global maximum rooting depth is derived from https://wci.earth2observe.eu/thredds/catalog/usc/root-depth/catalog.html. The tree density is derived from https://elischolar.library.yale.edu/yale_fes_data/1/. The forest age is downloaded from https://doi.org/10.17871/ForestAgeBGI.2021. The specific leaf area is downloaded from https://www.try-db.org/. The forest biomes were classified as DBF, ENF, and shrubland based on the European Space Agency/Climate Change Initiative Land Cover (ESA/CCI-LC) (http://maps.elie.ucl.ac.be/CCI/viewer/). The LAI was provided by MOD15A2H.061 (https://lpdaac.usgs.gov/products/mod15a2hv061/).

Research involving human participants, their data, or biological material

Policy information about studies with human participants or human data. See also policy information about sex, gender (identity/presentation), and sexual orientation and race, ethnicity and racism.

Reporting on sex and gender	N/A
Reporting on race, ethnicity, or other socially relevant groupings	N/A
Population characteristics	N/A
Recruitment	N/A
Ethics oversight	N/A

Note that full information on the approval of the study protocol must also be provided in the manuscript.

Field-specific reporting

Please select the one below that is the best fit for your research. If you are not sure, read the appropriate sections before making your selection.

☐ Life sciences ☐ Behavioural & social sciences ☒ Ecological, evolutionary & environmental sciences

For a reference copy of the document with all sections, see nature.com/documents/nr-reporting-summary-flat.pdf

Ecological, evolutionary & environmental sciences study design

All studies must disclose on these points even when the disclosure is negative.

Study description	We assessed post-mortality forest recovery rates for 1,699 well-documented forest mortality events across 1,600 sites that have occurred since the 1980s. Leveraging 158,427 Landsat images and extensive databases on global change factors, we quantified the time required for the examined sites' vegetation greenness (NDVI) and canopy water content (NDII) to return to pre-mortality levels and examined underlying mechanisms for recovery patterns. We demonstrate that (1) a slowing trend in forest recovery rate over the last three decades, especially between the 1990s and the 2000s; (2) the recovery of forest canopy water content significantly lagged that of vegetation greenness; (3) the slowing in global forest recovery were primarily due to warming and drought, with the escalation in the severity of forest mortality playing a much trivial role.
Research sample	The global dataset of tree mortality sites used in this study was obtained from multiple meta-analysis of previously reported tree mortality events. This dataset records the geo-referenced locations of 1,628 sites that document the timing of tree mortality events resulting from extreme drought and heat stress from 1970-2019.
Sampling strategy	N/A

Data collection	The Landsat-based NDVI and NDII, and DEM (including elevation, slope, and aspect) were calculated on Google Earth Engine, which is available at https://code.earthengine.google.com/. Other data sets were download from URLs that have been provided in the data availability statement in the main text.
Timing and spatial scale	We used 1,600 sites that document the timing of tree mortality events resulting from extreme drought and heat stress since the 1980s. These sites encompass a wide range of forest types and climate zones across all the continents except for Antarctica. For each of the 1,600 georeferenced sites, we calculated its corresponding mean value of NDVI and NDII of the growing season of each year from Landsat (30-m resolution, 1984-2020).
Data exclusions	We excluded 28 tree mortality sites from the 1970s from our analysis due to the lack of corresponding remote sensing data.
Reproducibility	Our analyses were based on publicly available satellite data, 1,600 geo-referenced tree mortality sites, and well-defined methods, and the results can be reliably reproduced.
Randomization	The XGBoost and SHAP models exhibited strong performance in simulating variations in recovery time for both NDVI and NDII during the procedures of cross validation (70% of samples for training the model while the remaining 30% for testing), making them suitable for exploring the major determinants of recovery time.
Blinding	N/A

Did the study involve field work? ☐ Yes ☒ No

Reporting for specific materials, systems and methods

We require information from authors about some types of materials, experimental systems and methods used in many studies. Here, indicate whether each material, system or method listed is relevant to your study. If you are not sure if a list item applies to your research, read the appropriate section before selecting a response.

Materials & experimental systems

n/a	Involved in the study
☒	☐ Antibodies
☒	☐ Eukaryotic cell lines
☒	☐ Palaeontology and archaeology
☒	☐ Animals and other organisms
☒	☐ Clinical data
☒	☐ Dual use research of concern
☒	☐ Plants

Methods

n/a	Involved in the study
☒	☐ ChIP-seq
☒	☐ Flow cytometry
☒	☐ MRI-based neuroimaging

Plants

Seed stocks	N/A
Novel plant genotypes	N/A
Authentication	N/A